NANO LETTERS

pubs.acs.org/NanoLett Letter

Strain Evolution in Nanocrystals under High Pressure Tracked with Bragg Coherent X-ray Diffraction Imaging

Abdelrahman Zakaria,* Sarah Yehya, Pierre Fertey, Björn Wehinger, Steven Leake, Mor Levi, Thomas W. Cornelius, Olivier Thomas, Mohamed Mezouar, Eugen Rabkin, Marie-Ingrid Richard, and Stéphane Labat

Cite This: *Nano Lett.* 2026, 26, 4807−4814 Read Online

ACCESS | Metrics & More | Article Recommendations | Supporting Information

ABSTRACT: Understanding stress accommodation at the atomic scale in nanocrystals is essential for operation in extreme environments. We use high-pressure Bragg Coherent Diffraction Imaging (BCDI) in a diamond anvil cell (DAC) to track three-dimensional strain and defects in individual platinum nanoparticles. The particle hosts an interfacial Shockley partial dislocation up to 2.7 GPa, followed at 5.0 GPa by nucleation of a dense dislocation network accompanied by anisotropic Bragg peak broadening, which later relaxes, indicating plasticity. Upon partial unloading, the interfacial partial reappears and transforms into a perfect dislocation that propagates into the crystal via cross-slip; additional glide events occur, while at 6.7 GPa anisotropic broadening re-emerges. Elastic finite-element modeling predicts shear stress concentrations near the particle−substrate interface, whereas nucleation is observed near the particle top surface. These results show that high-pressure BCDI captures dislocation activity and links reciprocal- and real-space signatures of plasticity in nanocrystals.

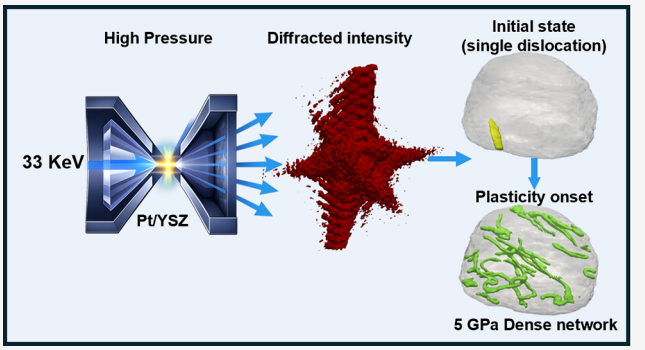

KEYWORDS: *Bragg coherent diffraction imaging, high pressure, dislocations, nanocrystals, plasticity, diamond anvil cell*

Understanding how nanocrystals respond to extreme conditions is a central challenge in materials science, with direct implications for catalysis, electronics, and structural reliability at the nanoscale. Under high pressure, nanocrystals provide a unique platform to probe elastic behavior, defect nucleation thresholds, and stress-driven transformations. Unlike bulk materials, nanocrystals exhibit strong surface effects, limited defect populations, and pronounced confinement, which can substantially modify their plastic response and stability.[1−4] The scarcity of dislocation sources and their interaction with free surfaces further promote source activation and early escape under load,[5] while size-dependent surface energy contributions additionally modulate mechanical stability.[6]

Among various approaches, high pressure applied using diamond anvil cells (DACs) provides a powerful means to explore material behavior across a wide range of stress states. High pressure enables access to metastable phases, anomalous mechanical responses, and pressure-driven transformations that are inaccessible at ambient conditions.[7−11] Resolving the microscopic mechanisms of these transformations in individual nanocrystals remains challenging and motivates the experimental approach shown in Figure 1.

Bragg coherent diffraction imaging (BCDI) is a non-destructive technique that visualizes strain fields and crystalline

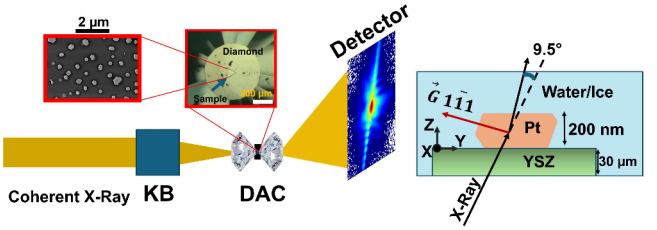

Figure 1. High-pressure BCDI setup at ESRF-ID27. A coherent X-ray beam focused by Kirkpatrick−Baez (KB) mirrors illuminates a Pt nanoparticle on a YSZ substrate inside a diamond anvil cell (DAC). Insets: (left) SEM image of the nanoparticle distribution on the substrate, (middle) optical micrograph of the DAC, and (right) schematic of the sample geometry and scattering configuration. The $(1\bar{1}1)$ Bragg reflection is accessed at a Bragg angle of $2\theta \approx 9.5°$, well within the DAC transmission aperture.

Received: February 2, 2026
Revised: March 19, 2026
Accepted: March 23, 2026
Published: April 2, 2026

https://doi.org/10.1021/acs.nanolett.6c00462
Nano Lett. 2026, 26, 4807−4814

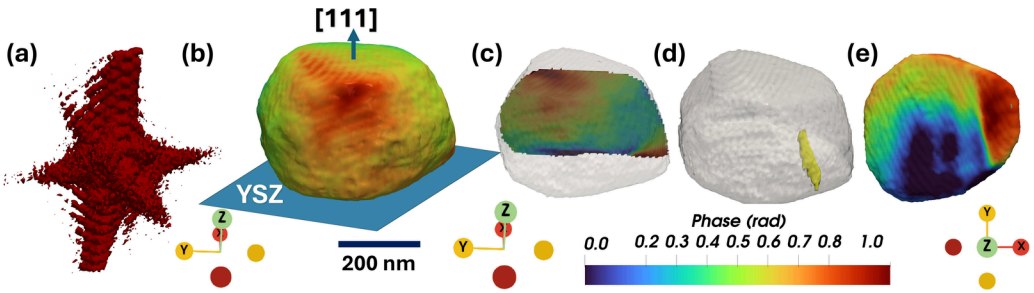

Figure 2. Initial state of the studied Pt nanoparticle at 0.3 GPa. (a) Three-dimensional coherent diffraction volume around the $1\bar{1}1$ Bragg peak (detector frame). (b) Surface-phase map (phase projected on the outer surface), highlighting a pronounced phase increase on the *top* (111) facet near its edge (red region). (c) Phase mapped on a cut of the outer surface, confirming the strong surface gradient across the top facet. (d) Reconstructed amplitude (morphology) with the segmented interfacial line defect (yellow), consistent with a Shockley partial dislocation pinned at the Pt−YSZ interface. (e) Surface-phase map from the opposite view emphasizing the strong phase variation on the *bottom* facet at the Pt−YSZ interface. Panels (a−d) are rendered from the same 3D viewing orientation to facilitate direct comparison; panel (e) shows the opposite view. Color bars show the phase (rad). Orientation triads refer to the orthogonalized laboratory frame. (Scale bar: 390 nm; particle dimensions ∼390 nm (lateral) × 240 nm (height).).

defects in three dimensions with nanometric resolution.[12−15] Reconstruction of the complex electron density provides the crystalline morphology from the amplitude and the lattice displacement field from the phase, $\phi(\mathbf{r}) = \mathbf{G}\cdot\mathbf{u}(\mathbf{r})$.[12,13,15] Here, $\mathbf{r}$ denotes the real-space position vector, $\mathbf{u}(\mathbf{r})$ is the lattice displacement field relative to the ideal crystal, and $\mathbf{G}$ is the reciprocal lattice vector corresponding to the measured Bragg reflection. The phase, therefore, encodes the projection of the displacement field along the scattering vector $\mathbf{G}$. Using hard X-rays at 33.170 keV enables transmission-mode BCDI through the diamond anvils of a DAC, extending coherent imaging to extreme-pressure environments where lower energies are strongly absorbed; this capability is made possible by the increased coherent flux of the ESRF Extremely Brilliant Source (EBS).

Pioneering high-pressure BCDI studies have demonstrated strain imaging and deformation mechanisms in Au and Ag nanocrystals compressed in diamond anvil cells.[16,17] However, these studies focused on freestanding nanocubes or weakly bonded nanocrystals. Here, we extend high-pressure BCDI to platinum and adopt a substrate-supported geometry in which Pt nanoparticles are strongly bonded to a yttria-stabilized zirconia (YSZ) substrate, providing realistic boundary conditions at the nanoparticle−substrate interface and directly influencing strain localization and defect nucleation under pressure.

Platinum is particularly significant in this context because it combines technological relevance with extensive use as a reference material in high-pressure experiments. Its mechanical stability, well-constrained equation of state, and high infrared absorption efficiency make Pt suitable for extreme-condition studies, while its elasticity, rheology, melting curve, and thermal properties under compression are well established.[18−21] Directly probing defect dynamics in Pt nanoparticles under high pressure with BCDI therefore provides a direct link between nanoscale plasticity and the broader high-pressure materials framework.

A platinum nanoparticle was characterized in its reference state at 0.3 GPa (Figure 2). The coherent 3D diffraction volume and real-space reconstructions reveal two key features: (i) a sharp interfacial phase discontinuity corresponding to a line defect pinned at the Pt-YSZ interface (Figure 2c,d), and (ii) pronounced surface-phase gradients on the external facets, most prominently on the *top* (111) facet near the $(1\bar{1}1)/(001)$ corner and on the *bottom* facet at the particle-substrate contact (Figure 2b,c,e). The particle measures ∼380 nm laterally and ∼240 nm in height, with the [111] axis normal to the substrate; dimensions and spatial resolution were verified by line cuts in Supporting Information, Section S8, (Figures S12−S15).

The interfacial discontinuity in Figure 2d exhibits a visible phase jump of ∼1 rad ($\approx \pi/3$). Because only one branch of the phase winding is observed at the interface, the true topological discontinuity is $\Delta\phi_{\text{true}} = 2\pi/3$, consistent with a Shockley partial dislocation. For $\mathbf{G} = \frac{2\pi}{a}[1\bar{1}1]$ and a Burgers vector of the form $\vec{b} = \frac{a}{6}\langle 112\rangle$, the expected phase jump satisfies $\Delta\phi = \mathbf{G}\cdot\vec{b} = 2\pi/3$, in agreement with the experiment.

Bragg-peak shifts were used to extract the average lattice strain as a function of pressure (Supplementary Figure S4), with colored bands indicating the phase of the pressure-transmitting medium. The strain-pressure response closely follows the bulk Pt equation of state reported by Kamada et al.[19] Using water as the pressure medium leads to solidification above ∼0.9 GPa and slight deviations from the hydrostatic reference, while the nanoparticle response remains predominantly elastic up to 7 GPa; the resulting non-hydrostaticity provides the shear stresses required to activate plasticity. Pressure was measured by ruby fluorescence;[22] the strain precision is set by the detector angular resolution and is $\sim 2 \times 10^{-4}$ (about 0.02%).

To visualize the pressure evolution of the Bragg peak, we computed maximum-intensity projections (MIPs) of the 3D diffraction pattern, defined as $I_{\text{MIP}}(Q_y, Q_z) = \max_{Q_x} I(Q_x, Q_y, Q_z)$, which emphasize anisotropic broadening while reducing background sensitivity. Figure 3 shows the MIP along Q_x in the orthogonalized laboratory frame; complementary projections are provided in Supplementary Figures S2 and S3.

The reciprocal-space evolution can be divided into four stages. Stage 1 (0.3−2.7 GPa) is characterized by a sharp and symmetric diffraction pattern, consistent with a predominantly elastic response, despite the presence of an interfacial Shockley partial dislocation that remains too localized to affect the Bragg peak shape. At Stage 2 (5.0 GPa), a sudden anisotropic broadening appears as a streak inclined by ∼30° from Q_z toward $+Q_y$, indicating a marked increase in internal strain

https://doi.org/10.1021/acs.nanolett.6c00462
Nano Lett. 2026, 26, 4807−4814

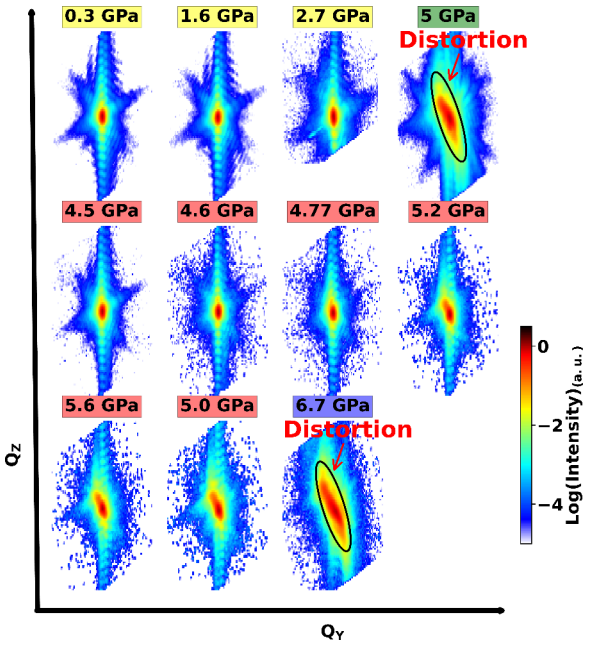

Figure 3. Maximum-intensity projection (MIP) of the 3D diffraction pattern during compression, computed as $I_{MIP}(Q_y, Q_z) = \max_{Q_x} I(Q_x, Q_y, Q_z)$ in the orthogonalized laboratory frame. Anisotropic broadening appears at 5 GPa (Stage 2) along the crystal [131] direction, partially recovers at 4.5 GPa (Stage 3), and intensifies again at 6.7 GPa (Stage 4).

heterogeneity. Using the orientation matrix from the initial-state reconstruction, this distortion maps to the crystal [131] direction. Upon partial unloading, Stage 3 (4.5−5.6 GPa) shows a substantial recovery of the diffraction pattern toward its low-pressure morphology, followed by the gradual re-emergence of the same directional broadening during recompression, demonstrating its reproducibility. At Stage 4 (6.7 GPa), pronounced anisotropic broadening reappears consistent with a highly inhomogeneous strain field.

The reproducibility of the distorted and undistorted states was confirmed by three-dimensional Pearson cross-correlation analysis of the diffraction volumes (Supplementary Figure S8). Direction-resolved peak-shape metrics extracted from one-dimensional profiles further quantify the reversible, anisotropic broadening along the [131] direction (Supporting Information, Section S4; Figures S6−S7).

Real-space phase reconstructions complement the reciprocal-space findings by directly visualizing the evolution of strain and defect structures inside the nanoparticle. The reconstructions reveal numerous dislocation segments and looplike features, providing a microscopic origin for the highly inhomogeneous strain field inferred from the diffraction-pattern analysis—namely the directional broadening and intensity redistribution in Figure 3 (and the stage-wise similarity in Supplementary Figure S8). Figure 4 summarizes the entire pressure cycle, showing the dislocation network and its evolution. The dislocation-line extraction and segmentation workflow is described in Supporting Information, Section S11.

Stage 1 (0.3−2.7 GPa): Stable Interfacial Partial Dislocation

At low pressure, as mentioned before, the sharp phase discontinuity observed at the interface with the substrate can be attributed to a Shockley partial dislocation. When the

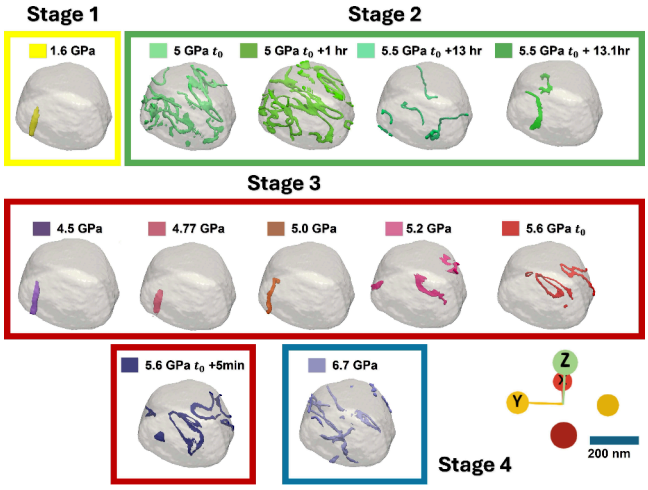

Figure 4. Segmented 3D dislocation structures at each pressure scan. Color code corresponds to the pressure stages: Stage 1 (yellow), Stage 2 (green), Stage 3 (red), Stage 4 (blue). The evolution includes persistence of the initial partial dislocation, emergence of dense defect networks, and loop gliding.

pressure is increased up to 2.7 GPa, the transformation of liquid water into solid ice VI, predicted at 0.9 GPa, does not affect the nanoparticle. Similarly, the transformation into ice VII, expected at 2.1 GPa, has no effect on platinum. The defect remains pinned at the interface and stable throughout Stage 1. This contrasts with the earlier high-pressure BCDI study on freestanding silver nanocubes dispersed in water by Huang et al.,[17] where the particles were highly unstable below 2.1 GPa, likely due to the absence of a substrate to mechanically stabilize them.

Stage 2 (5.0−5.5 GPa): Onset of Defect Proliferation

At 5.0 GPa, the real-space reconstruction reveals a marked transformation of the defect structure relative to Stage 1. Whereas the Shockley partial dislocation remained pinned at the Pt−substrate interface up to 2.7 GPa, a dense, complex defect network appears is first observed at Stage 2, including curved dislocation lines and looplike features. Such looplike signatures are consistent with prior BCDI observations of prismatic dislocation loops nucleated at the onset of plasticity in nanocrystals.[23,24] Additional phase slices and angular phase analyzes around dislocation cores are provided in Supporting Information, Section S6 (Figures S10−S14).

Because no intermediate pressure points were acquired between 2.7 and 5.0 GPa during the initial loading, the precise onset pressure of network formation cannot be resolved from Stage 1−2 alone, and 5.0 GPa should be regarded as an upper bound for its emergence. This limitation is mitigated by Stage 3, where smaller pressure steps during unloading/reloading (4.5−5.6 GPa) capture reversible broadening and repeated defect activity near 5 GPa, consistent with a plasticity threshold in this range.

Moreover, under constant pressure conditions (set to 5.0 GPa), the network evolves markedly with time: after ∼1 h it continues to reorganize and grow, whereas after ∼13 h most segments have relaxed or annihilated and only a few dislocations remain. Although the applied load did not change during the period, pressure calibration at the end of the measurement indicated a slight increase to ∼5.5 GPa. This slow time dependence indicates sustained, continuous plastic activity under load rather than a single abrupt event. The

https://doi.org/10.1021/acs.nanolett.6c00462
Nano Lett. 2026, 26, 4807−4814

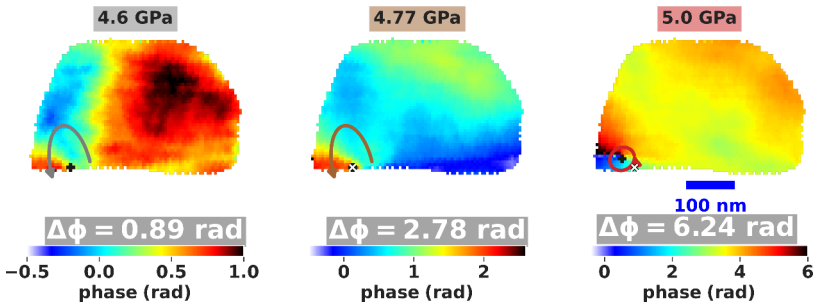

Figure 5. Phase slices intersecting the same dislocation line during Stage 3. At 4.6 GPa (left), the interfacial partial reappears with a visible phase jump of $\Delta\phi$ = 0.90 rad. At 4.77 GPa (middle), the discontinuity increases to $\Delta\phi$ = 2.84 rad, approaching a full dislocation. At 5.0 GPa (right), the defect has transformed into a perfect dislocation with $\Delta\phi$ = 6.09 rad and has migrated into the particle volume. Ellipses highlight the defect cores, while the cross marks the position of the initial interfacial dislocation for reference. Note that color scales differ between panels (see individual bars).

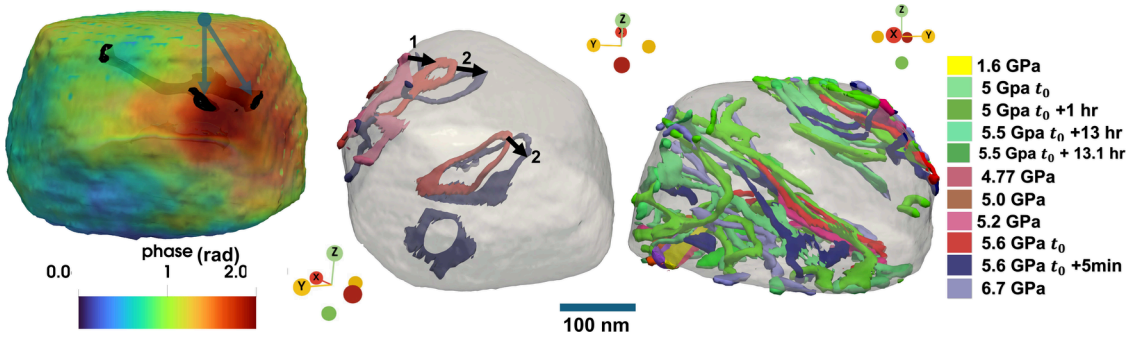

Figure 6. Surface nucleation and subsequent glide of dislocations during Stage 3. Left: surface-phase map at 5.0 GPa (Stage 3, t_0) overlaid with the dislocation line at 5.2 GPa ($t_0 + \Delta t$). A dislocation nucleates at a region of highest surface phase near a multifacet intersection and propagates into the crystal. Center: early Stage 3 snapshots tracing the initial trajectory of the nucleated defect. Arrow 1: glide into the volume and loop formation during the first scan at 5.6 GPa. Arrow 2: continued glide of the two loop segments toward the Pt-YSZ interface in the subsequent scan at 5.6 GPa. Right: cumulative map of all segmented dislocations across the pressure cycle, color-coded by pressure, revealing multiple glide events and the emergence of a dislocation-free band with an apparent orientation close to the (131) plane. This orientation should not be interpreted as slip on (131), but rather reflects the apparent alignment of dislocation cores within the spatial resolution of BCDI, consistent with the anisotropic broadening direction $\mathbf{G} = [1\bar{1}1]$ observed in reciprocal space.

gradual annihilation of dislocations at constant pressure most likely reflects thermally activated unpinning from locks, while the presence of other dislocations invisible in the measured Bragg reflection may also act as barriers and influence the relaxation dynamics.

Stage 3 (4.5−5.6 GPa): Recovery and Transformation

After a partial unloading, the same interfacial partial reappears at 4.5−4.6 GPa with an identical $\pi/3$ phase jump, demonstrating full reversibility of the initial defect (Figure 5, left). At 4.77 GPa, however, the discontinuity increases to nearly π, corresponding to the formation of a perfect dislocation (Figure 5, middle). The mechanism behind this transformation is not unambiguously resolved. One possibility is that the observed perfect dislocation corresponds to the sum of two Shockley partial dislocations, as can be verified from Thompson's tetrahedron decomposition. As described in Supporting Information, Section S7 (Table S2), a second Shockley partial dislocation emitted at the Pt−YSZ interface can react with the pre-existing interfacial partial to form a perfect $a/2\langle 110\rangle$ segment. Importantly, such a "perfect" line may remain dissociated into two $a/6\langle 112\rangle$ partials whose separation is smaller than our real-space resolution (~15 nm), so the two cores cannot be resolved in the present reconstructions. In both cases, by 5.0 GPa the defect behaves as a mobile dislocation that migrates into the particle volume (Figure 5, right).

Although the dominant segment appears to slip approximately along the (131) plane, no conventional $a/2\langle 110\rangle$ Burgers vector lies in (131) and satisfies the visibility condition ($\mathbf{G}\cdot\mathbf{b} \neq 0$). We therefore interpret the slide path as an *effective* envelope produced by intermittent glide on neighboring {111} planes—via cross-slip.[25,26] The defect unambiguously slips upward, away from the Pt−YSZ interface.

To connect the onset of defect activity with the surface strain field, Figure 6 (left) overlays the phase mapped on the particle surface at 5.0 GPa with the dislocation line extracted at 5.2 GPa. The first dislocation segment nucleates exactly at the region of *maximum surface phase* (red) located at the intersection of several facets, then penetrates into the volume. This spatial coincidence indicates that the local surface strain concentration acts as the nucleation site under pressure.

Following the nucleation at 5.0 GPa (Figure 6 (left)), the first scan at 5.6 GPa already shows *two* dislocation loops: (i) the loop inherited from the 5.2 GPa segment, and (ii) a second loop that forms approximately in the middle of the particle. Arrow **1** in Figure 6 (center) marks the glide and loop-closure captured in this first scan at 5.6 GPa. In the subsequent scan at the same nominal pressure, both loops/loop segments slip downward toward the Pt−YSZ interface (Arrow **2**), i.e. away from the top surface, migrating from regions of high stress

https://doi.org/10.1021/acs.nanolett.6c00462
Nano Lett. 2026, 26, 4807−4814

toward lower-stress regions at the interface, consistent with the behavior described in ref 27. Most of the dominant defect segments are oriented close to the (131) plane. We stress that this does not imply that (131) is the actual slip plane; rather, the reconstructed dislocation cores project near this orientation within the resolution of BCDI. Similar anomalous orientations of defect segments have been reported previously in platinum.[28]

The normal to the (131) plane, [131], coincides with the crystallographic direction of the anisotropic broadening observed in reciprocal space (Figure 6 (right)), reinforcing the consistency between real- and reciprocal-space signatures.

In addition, the cumulative defect maps (Figure 6 (right)) exhibit a striking dislocation-free band approximately coincident with the (131) plane. For $\mathbf{G} = [1\bar{1}1]$, one would instead expect a nanotwin bounded by the $(1\bar{1}1)$ plane, as reported previously in Pt nanoparticles.[29]

The observed band and the expected twin orientation do not coincide, yet both can be reconstructed under a common Bragg peak due to the projection inherent to single-reflection BCDI. This mismatch leaves the precise nature of the defect-free band an open question.

A complete scan-by-scan overview of pressure and defect activity is summarized in Supporting Information, Figure S11.

To rationalize the observed defect activity, we performed elastic finite element simulations of a platinum nanoparticle supported on a YSZ substrate and subjected to 5 GPa hydrostatic compression (see Supporting Information, Section S7; Figures S15–S16 and Table S3). The model isolates the elastic effect of substrate support under nominally hydrostatic loading and should therefore be regarded as a zeroth-order approximation. Although the applied load is nominally hydrostatic, the simulations reveal strong stress inhomogeneities arising from the presence of the substrate, breaking the hydrostatic symmetry. In particular, resolved shear stresses (RSS) concentrate near the particle–substrate interface.

The maximum RSS reaches about 500 MPa, corresponding to a normalized value of $\mathrm{RSS}/\mu \approx 0.008$ (with $\mu = 61$ GPa for Pt). This lies within the lower bound of the critical resolved shear stress (CRSS) reported for Pt nanoparticles,[30,31] indicating that the applied pressure is sufficient to trigger plastic activity. However, the highest stresses are localized at the interface. This does not agree with the experimental observation of nucleation at the top surface.

We therefore conclude that plasticity in supported nanoparticles is governed not only by the induced shear stress arising from nonhydrostatic concentrations at the substrate, but also by the additional confinement imposed by the surrounding solidified ice in contact with the particle and substrate, as well as by other factors leading to stress concentration at the edges of the top particle facets. In this respect, it should be noted that the Pt particles studied in the present work were obtained by solid-state dewetting of thin Pt films in air. At the dewetting temperature of 1000 °C, some evaporation of Pt occurs, resulting in particles of various shapes that deviate from the equilibrium Wulff construction.[32] Close inspection of Figure S1 in Supporting Information, reveals that the top facets of some Pt particles exhibit sharp edges. Formally, such edges can be described as smoothly curved surface patches with a small radius of curvature r. For r of the order of 10 nm, the corresponding capillary stress can be estimated as $\Gamma/r \approx 240$ MPa, where $\Gamma = 2.4$ J/m^2 is the surface energy of Pt. In smaller nanoparticles, such capillary stresses at the facet edges were shown to result in spontaneous dislocation nucleation.[33] An additional contribution to the stress concentration at the particle top facet comes from confinement imposed by the surrounding solidified ice.

Moreover, approximate estimates of the Peach–Koehler force acting on the interfacial dislocation line, based on our elastic FEM simulations of a defect-free particle, indicate that the line should be attracted toward the interface rather than propagating upward toward the top surface. The experimentally observed nucleation at the top surface and upward glide therefore indicate that additional mechanisms, not included in the present elastic baseline model, contribute to the stress state. These may include confinement-induced stress anisotropy from the surrounding solidified pressure medium, capillary stresses associated with sharp facet edges, image forces near the free surface, and possible nonuniform pressure gradients within the DAC environment. Incorporating such effects would require a multiphysics treatment beyond the scope of the present Letter.

This work demonstrates how Bragg Coherent Diffraction Imaging under high pressure provides unique insight into defect dynamics in individual nanocrystals. The nanoparticle studied here passes through four distinct stages: (i) a stable interfacial Shockley partial dislocation up to 2.7 GPa; (ii) the onset of plasticity first observed at 5.0 GPa, with a time-dependent dislocation network that reorganizes and partially relaxes under sustained load; (iii) reproducible recovery of the interfacial partial upon unloading, followed by its transformation into a perfect dislocation and cross-slip mediated glide, alongside nucleation of new loops from surface hot spots; and (iv) renewed anisotropic distortion at 6.7 GPa, with the appearance of a dislocation-free band whose nature remains unresolved.

The combined reciprocal- and real-space analyses establish the reproducibility of directional broadening along [131] and directly link it to dislocation activity. Elastic finite-element simulations confirm strong stress concentrations near the particle-substrate interface but cannot account for the observed upward glide of dislocations, indicating that plasticity in supported nanoparticles is governed not only by substrate-induced shear stress and confinement by the solidified pressure medium but also by additional mechanisms such as cross-slip, partial–perfect reactions, and defect interactions.

By capturing the nucleation, transformation, and mobility of dislocations under hydrostatic loading, this study highlights the power of high-pressure BCDI to reveal the microscopic origins of plasticity in confined nanocrystals and sets the stage for future work combining multireflection BCDI with full strain-tensor reconstruction.

Sample Synthesis

Platinum nanoparticles were prepared on YSZ (001) substrates by solid-state dewetting. A 15 nm Pt film was sputtered onto polished substrates and annealed at 1000 °C in air for 1 h, inducing agglomeration into faceted single crystals with typical dimensions of ∼240 nm (height) and ∼380 nm (lateral). The YSZ lamella thickness was ∼30 μm, enabling transmission-mode X-ray diffraction in the DAC. Particles show a preferential [111] orientation normal to the substrate and are sufficiently isolated for coherent diffraction imaging.

High-Pressure Loading

Samples were loaded in a panoramic diamond anvil cell (DAC) equipped with 300 μm culets and a preindented

https://doi.org/10.1021/acs.nanolett.6c00462
Nano Lett. 2026, 26, 4807–4814

stainless-steel gasket. Distilled water was used as the pressure-transmitting medium and solidifies near 0.9 GPa. Pressure was calibrated by ruby fluorescence (Figure 1). Although solidified water develops nonhydrostatic stresses at the macroscopic scale, the nanoparticles studied here are only a few hundred nanometers in size.

Bragg Coherent Diffraction Imaging

Experiments were performed at ESRF beamline ID27 in transmission geometry using a monochromatic X-ray beam at 33.170 keV. The beamline optics comprised a double multilayer mirror system, a Si(111) monochromator, and Kirkpatrick-Baez mirrors for focusing. Upstream slits were set to 200 × 60 μm^2 (H × V), producing a focal spot of ∼0.7 × 0.7 μm^2 at the sample and transverse coherence lengths of ∼58 μm (horizontal) and ∼438 μm (vertical). Diffraction from individual Pt nanoparticles was measured at the $1\bar{1}1$ Bragg reflection using an Eiger2 9 M CdTe detector (75 μm pixels, 750 μm sensor) positioned 2.65 m downstream. Three-dimensional data sets were acquired by rocking the sample over 1.0° in 201 steps of 0.005° with 1 s exposure per frame (∼200 s per data set). This acquisition time is short compared with the defect dynamics discussed in the Results, allowing each reconstruction to be treated as quasi-static. Pressure was measured by ruby fluorescence. Additional details of the ID27 beamline are given in ref.[34]

Phase Retrieval

Diffraction data were reconstructed using PyNX[35] with iterative hybrid input-output (HIO) and error-reduction (ER) algorithms. In-house Python scripts were used for preprocessing (masking, centering, background subtraction), workflow orchestration, and visualization. Complex real-space reconstructions were obtained, and lattice displacement fields were extracted from the phase. Additional details of preprocessing and centering are provided in Supporting Information, Section S8. Support constraints were updated dynamically in most reconstructions. For data sets with complex diffraction patterns, corresponding to Stage 2 (5.0 GPa) and Stage 4 (6.7 GPa), a fixed support was used to stabilize convergence. At 5.6 GPa, a mixed strategy was applied, with an initially fixed support followed by updates after a defined number of iterations to refine the morphology while maintaining convergence.

Finite Element Modeling

Elastic simulations were performed in COMSOL using anisotropic elasticity for both the Pt nanoparticle and the YSZ substrate. The nanoparticle geometry (380 nm × 380 nm base, 240 nm height) was placed on a 2000 nm-thick YSZ slab. A uniform hydrostatic pressure of 5 GPa was applied to all exposed surfaces, with fixed nodes at the bottom of the substrate to suppress rigid-body motion. Pt elastic constants were C_{11} = 345 GPa, C_{12} = 250 GPa, and C_{44} = 75 GPa, while YSZ was described by C_{11} = 400 GPa, C_{12} = 100 GPa, and C_{44} = 60 GPa. Stiffness tensors were rotated into the experimental frame ($X \| [2\bar{1}\bar{1}]$, $Y \| [01\bar{1}]$, $Z \| [111]$), and the resulting stress fields were projected onto FCC slip systems to compute resolved shear stress (RSS) for comparison with BCDI observations.[36]

■ ASSOCIATED CONTENT

Data Availability Statement

The coherent diffraction data sets and reconstruction outputs generated in this study are available at the ESRF data repository (DOI: 10.15151/ESRF-ES-1215139768). All data were collected during the ESRF experiment HC-5272 at beamline ID27. Processed figures and additional derived data are provided within the article and its Supporting Information. Custom Python scripts used for data processing and visualization are openly available at https://github.com/Abdzak/cdi_dislo. Phase retrieval was performed with PyNX;[35] utilities from cdiutils[37] were used where indicated in the repository.

Supporting Information

The Supporting Information is available free of charge at https://pubs.acs.org/doi/10.1021/acs.nanolett.6c00462.

Sample overview and SEM imaging (S1); additional orthogonal maximum-intensity projections of the 3D diffraction patterns (S2); average lattice strain versus pressure compared with the Pt equation of state (S3); definitions and evolution of diffraction peak-shape metrics including fwhm, integral breadth, skewness, and kurtosis (S4); three-dimensional cross-correlation analysis of diffraction volumes (S5); real-space resolution estimates and a scan-by-scan pressure timeline (S6); Burgers-vector visibility and {111} dissociation relations for $\mathbf{G} = [1\bar{1}1]$ (S7); additional phase slices, dislocation-loop views, angular phase analyses, and defect-trajectory renderings (S8); finite element simulation geometry, stress and resolved shear stress (RSS) maps with summary values (S9); the complete data-processing workflow (S10); the phase-offset minimization strategy for defect identification (S11); and a summary of software tools used for reconstruction and analysis (S12) (PDF)

3D visualization of the nucleation and early evolution of a dislocation at the top facet during Stage 3, followed by two glide events (GIF)

3D visualization of the cumulative dislocation network over all pressure stages (GIF)

3D visualization of the dislocation segments associated with the glide events observed during Stage 3 (GIF)

■ AUTHOR INFORMATION

Corresponding Author

Abdelrahman Zakaria − *Aix-Marseille Université, Université de Toulon, 13397 Marseille, France;* orcid.org/0000-0003-1489-3359; Email: abdelrahman.zakaria@cea.fr

Authors

Sarah Yehya − *Aix-Marseille Université, Université de Toulon, 13397 Marseille, France*

Pierre Fertey − *Synchrotron SOLEIL, Saint-Aubin 91190, France*

Björn Wehinger − *European Synchrotron Radiation Facility, CS 38043 Grenoble, France*

Steven Leake − *European Synchrotron Radiation Facility, CS 38043 Grenoble, France*

Mor Levi − *Department of Materials Science and Engineering, Technion, 3200003 Haifa, Israel*

https://doi.org/10.1021/acs.nanolett.6c00462
Nano Lett. 2026, 26, 4807−4814

Thomas W. Cornelius − *Aix-Marseille Université, Université de Toulon, 13397 Marseille, France;* orcid.org/0000-0003-4272-4720
Olivier Thomas − *Aix-Marseille Université, Université de Toulon, 13397 Marseille, France*
Mohamed Mezouar − *European Synchrotron Radiation Facility, CS 38043 Grenoble, France;* orcid.org/0000-0001-5336-544X
Eugen Rabkin − *Department of Materials Science and Engineering, Technion, 3200003 Haifa, Israel;* orcid.org/0000-0001-5545-1261
Marie-Ingrid Richard − *Université Grenoble Alpes, CEA Grenoble, 38000 Grenoble, France;* orcid.org/0000-0002-8172-3141
Stéphane Labat − *Aix-Marseille Université, Université de Toulon, 13397 Marseille, France*

Complete contact information is available at: https://pubs.acs.org/10.1021/acs.nanolett.6c00462

Author Contributions

Abdelrahman Zakaria (AZ) and Sarah Yehya (SY) conceived and designed the study, carried out data processing, and performed the phase retrieval (AZ leading the reconstructions with PyNX). The BCDI experiment at ESRF-ID27 was performed by AZ, SY, Björn Wehinger (BW), Mohamed Mezouar (MM), Steven Leake (SL), Pierre Fertey (PF), and Marie-Ingrid Richard (M-IR). Eugen Rabkin (ER) and Mor Levi (ML) contributed to sample preparation. AZ and SY performed the formal analysis and visualization. Thomas Cornelius (TC), Olivier Thomas (OT), Stéphane Labat (S. Labat), M-IR, and SL provided scientific guidance and interpretation. AZ drafted the manuscript with input from all authors. All authors discussed the results and approved the final manuscript.

Funding

This work was supported by the French National Research Agency (ANR) under grant ANR-21-CE08-0033 (DINACS project). This project received funding from the European Research Council (ERC) under the European Union's Horizon 2020 research and innovation program (grant agreement No. 818823).

Notes

The authors declare no competing financial interest.

■ ACKNOWLEDGMENTS

We gratefully acknowledge the European Synchrotron Radiation Facility (ESRF) for beamtime under proposal HC-5272 and the dedicated support of the ID27 beamline staff. All scientists involved in the beamtime contributed to the commissioning and performance of the BCDI experiments. In particular, we thank Sébastien Petit-Demange for ensuring the proper operation of the control system and for his help in adapting the ID01 macros for use at ID27. We also thank Jeroen Jacobs for the preparation of the diamond anvil cells.

■ REFERENCES

(1) Greer, J. R.; Oliver, W. C.; Nix, W. D. Size dependence of mechanical properties of gold at the micron scale in the absence of strain gradients. *Acta Mater.* **2005**, *53*, 1821−1830.
(2) Uchic, M. D.; Dimiduk, D. M.; Florando, J. N.; Nix, W. D. Sample dimensions influence strength and crystal plasticity. *Science* **2004**, *305*, 986−989.
(3) Volkert, C. A.; Lilleodden, E. T. Size effects in the deformation of sub-micron Au columns. *Philos. Mag.* **2006**, *86*, 5567−5579.
(4) Brenner, S. S. Tensile Strength of Whiskers. *J. Appl. Phys.* **1956**, *27*, 1484.
(5) Oh, S. H.; Legros, M.; Kiener, D.; Dehm, G. In situ observation of dislocation nucleation and escape in a submicrometre aluminium single crystal. *Nature materials* **2009**, *8*, 95−100.
(6) Vollath, D.; Fischer, F. D.; Holec, D. Surface energy of nanoparticles−influence of particle size and structure. *Beilstein journal of nanotechnology* **2018**, *9*, 2265−2276.
(7) Guillaume, C. L.; Gregoryanz, E.; Degtyareva, O.; McMahon, M. I.; Hanfland, M.; Evans, S.; Guthrie, M.; Sinogeikin, S. V.; Mao, H.-K. Cold melting and solid structures of dense lithium. *Nat. Phys.* **2011**, *7*, 211−214.
(8) Sun, L.; et al. Re-emerging superconductivity at 48 K in iron chalcogenides. *Nature* **2012**, *483*, 67−69.
(9) Somayazulu, M.; Dera, P.; Goncharov, A. F.; Gramsch, S. A.; Liermann, P.; Yang, W.; Liu, Z.; Mao, H.-k.; Hemley, R. J. Pressure-induced bonding and compound formation in xenon−hydrogen solids. *Nat. Chem.* **2010**, *2*, 50−53.
(10) Loubeyre, P.; Occelli, F.; Dumas, P. Synchrotron infrared spectroscopic evidence of the probable transition to metal hydrogen. *Nature* **2020**, *577*, 631−635.
(11) Eremets, M. I.; Troyan, I. A. Conductive dense hydrogen. *Nat. Mater.* **2011**, *10*, 927−931.
(12) Robinson, I.; Harder, R. Coherent X-ray diffraction imaging of strain at the nanoscale. *Nat. Mater.* **2009**, *8*, 291−298.
(13) Pfeifer, M.; Williams, G.; Vartanyants, I.; Harder, R.; Robinson, I. Three-dimensional mapping of a deformation field inside a nanocrystal. *Nature* **2006**, *442*, 63−66.
(14) Harder, R.; Pfeifer, M. A.; Williams, G. J.; Vartaniants, I. A.; Robinson, I. K. Orientation variation of surface strain. *Phys. Rev. B* **2007**, *76*, 115425.
(15) Newton, M.; Leake, S.; Harder, R.; Robinson, I. Three-dimensional strain in a single ZnO nanorod. *Nat. Mater.* **2010**, *9*, 120−124.
(16) Yang, W.; Huang, X.; Harder, R.; Clark, J. N.; Robinson, I. K.; Mao, H.-k. Coherent diffraction imaging of nanoscale strain evolution in a single crystal under high pressure. *Nat. Commun.* **2013**, *4*, 1680.
(17) Huang, X.; Yang, W.; Harder, R.; Sun, Y.; Lu, M.; Chu, Y. S.; Robinson, I. K.; Mao, H.-k. Deformation Twinning of a Silver Nanocrystal under High Pressure. *Nano Lett.* **2015**, *15*, 7644−7649.
(18) Kavner, A.; Duffy, T. S. Elasticity and rheology of platinum under high pressure. *Phys. Rev. B* **2003**, *68*, 144101.
(19) Kamada, S.; Fukui, H.; Yoneda, A.; Gomi, H.; Maeda, F.; Tsutsui, S.; Uchiyama, H.; Hirao, N.; Ishikawa, D.; Baron, A. Q. R. Elastic constants of single-crystal Pt measured up to 20 GPa based on inelastic X-ray scattering: Implication for the establishment of an equation of state. *Comptes Rendus Geoscience* **2019**, *351*, 236−242. High-Pressure Mineral Physics Seminar (HPMPS-9, Saint-Malo, France, 24−28 September 2017).
(20) Anzellini, S.; Monteseguro, V.; Bandiello, E.; Dewaele, A.; Burakovsky, L.; Errandonea, D. In situ characterization of the high P−T melting curve of platinum. *Sci. Rep.* **2019**, *9*, 13034.
(21) Hasegawa, A.; Ohta, K.; Yagi, T.; Hirose, K. Thermal conductivity of platinum and periclase under extreme conditions of pressure and temperature. *High Pressure Research* **2023**, *43* (1), 68−80.
(22) Mao, H. K.; Xu, J.; Bell, P. M. Calibration of the ruby pressure gauge to 800 kbar under quasi-hydrostatic conditions. *Journal of Geophysical Research: Solid Earth* **1986**, *91*, 4673−4676.
(23) Dupraz, M.; Beutier, G.; Cornelius, T. W.; Parry, G.; Ren, Z.; Labat, S.; Richard, M.-I.; Chahine, G. A.; Kovalenko, O.; De Boissieu, M.; Rabkin, E.; Verdier, M.; Thomas, O. 3D Imaging of a Dislocation Loop at the Onset of Plasticity in an Indented Nanocrystal. *Nano Lett.* **2017**, *17*, 6696.
(24) Yehya, S.; Cornelius, T. W.; Richard, M.-I.; Berenguer, F.; Levi, M.; Rabkin, E.; Thomas, O.; Labat, S. In situ three-dimensional

observation of plasticity onset in a Pt nanoparticle. *Nanoscale* **2024**, *16*, 20670−20678.
(25) Hirth, J.; Lothe, J. *Theory of Dislocations*; John Wiley & Sons, 1982.
(26) Rodney, D.; Proville, L. Stress-dependent activation enthalpy for cross slip in fcc metals from atomistic calculations. *Phys. Rev. B* **2009**, *79*, 094108.
(27) Lee, S.; Im, J.; Yoo, Y.; Bitzek, E.; Kiener, D.; Richter, G.; Kim, B.; Oh, S. H. Reversible cyclic deformation mechanism of gold nanowires by twinning−detwinning transition evidenced from *in situ* TEM. *Nat. Commun.* **2014**, *5*, 3033.
(28) Richard, M.-I.; et al. Anomalous Glide Plane in Platinum Nano- and Microcrystals. *ACS Nano* **2023**, *17*, 6113−6120.
(29) Carnis, J.; Kshirsagar, A. R.; Wu, L.; Dupraz, M.; Labat, S.; Texier, M.; Favre, L.; Gao, L.; Oropeza, F. E.; Gazit, N.; Almog, E.; Campos, A.; Micha, J.-S.; Hensen, E. J. M.; Leake, S. J.; Schulli, T. U.; Rabkin, E.; Thomas, O.; Poloni, R.; Hofmann, J. P.; Richard, M.-I. Twin boundary migration in an individual platinum nanocrystal during catalytic CO oxidation. *Nat. Commun.* **2021**, *12*, 5385.
(30) Zimmerman, J.; Bisht, A.; Mishin, Y.; Rabkin, E. Size and shape effects on the strength of platinum nanoparticles. *J. Mater. Sci.* **2021**, *56*, 18300−18312.
(31) Azadehranjbar, S.; Ding, R.; Padilla Espinosa, I. M.; Martini, A.; Jacobs, T. D. B. Size-dependent role of surfaces in the deformation of platinum nanoparticles. *ACS Nano* **2023**, *17*, 8133−8140.
(32) Ringe, E.; Van Duyne, R. P.; Marks, L. D. Kinetic and Thermodynamic Modified Wulff Constructions for Twinned Nanoparticles. *J. Phys. Chem. C* **2013**, *117*, 15859−15870.
(33) Diao, J.; Gall, K.; Dunn, M. L. Surface-stress-induced phase transformation in metal nanowires. *Nat. Mater.* **2003**, *2*, 656−660.
(34) Mezouar, M.; Garbarino, G.; Bauchau, S.; Morgenroth, W.; Martel, K.; Petitdemange, S.; Got, P.; Le Godec, Y.; Kantor, I.; Bossak, A.; Hanfland, M.; Crichton, W.; Wehinger, B. The High Flux Nano-X-Ray Diffraction, Fluorescence and Imaging Beamline ID27 for Science under Extreme Conditions on the ESRF Extremely Brilliant Source. *High Pressure Research* **2024**, *44*, 171−198.
(35) Favre-Nicolin, V.; Girard, G.; Leake, S.; Carnis, J.; Chushkin, Y.; Kieffer, J.; Paleo, P.; Richard, M.-I. PyNX: high-performance computing toolkit for coherent X-ray imaging based on operators. *J. Appl. Crystallogr.* **2020**, *53*, 1404−1413.
(36) Simmons, G.; Wang, H. *Single Crystal Elastic Constants and Calculated Aggregate Properties: A Handbook*; MIT Press: Cambridge, MA, 1971; ISBN 9780262190963.
(37) Atlan, C. Cdiutils: A python package for Bragg Coherent Diffraction Imaging processing, analysis and visualisation workflows, 2025. DOI: 10.5281/zenodo.14894468.

https://doi.org/10.1021/acs.nanolett.6c00462
Nano Lett. 2026, 26, 4807−4814